



Efficient NH₃-SCR removal of NO_x with highly ordered mesoporous WO₃(χ)-CeO₂ at low temperatures

Sihui Zhan ^{a,*}, He Zhang ^a, Yu Zhang ^a, Qiang Shi ^a, Yi Li ^b, XiuJun Li ^{c,*}

^a College of Environmental Science and Engineering, Nankai University, Tianjin 300071, PR China

^b Department of Chemistry, Tianjin University, Tianjin 300072, PR China

^c Department of Chemistry, University of Texas at El Paso, El Paso, TX 79968, USA



ARTICLE INFO

Article history:

Received 26 July 2016

Received in revised form 1 October 2016

Accepted 7 October 2016

Available online 13 October 2016

Keywords:

NO_x removal

Highly-ordered mesoporous

W-Ce oxides

Low temperature SCR

ABSTRACT

To eliminate nitrogen oxides (NO_x), a series of highly ordered mesoporous WO₃(χ)-CeO₂ nanomaterials (χ represents the mole ratio of W/Ce) were synthesized by using KIT-6 as a hard template, which was used for selective catalytic reduction (SCR) to remove NO_x with NH₃ at low temperatures. Moreover, the nanomaterials were characterized by TEM, XRD, Raman, XPS, BET, H₂-TPR, NH₃-TPD and *in situ* DRIFTS. It can be found that all of the prepared mesoporous WO₃(χ)-CeO₂ (χ = 0, 0.5, 0.75, 1 and 1.25) showed highly ordered mesoporous channels. Furthermore, mesoporous WO₃(1)-CeO₂ exhibited the best removal efficiency of NO_x, and its NO_x conversion ratio could reach 100% from 225 °C to 350 °C with a gas hourly space velocity of 30 000 h⁻¹, which was due to higher Ce³⁺ concentrations, abundant active surface oxygen species and Lewis acid sites based on XPS, H₂-TPR, NH₃-TPD and *in situ* DRIFTS. In addition, several key performance parameters of mesoporous WO₃(1)-CeO₂, such as superior water resistance, better alkali metal resistance, higher thermal stability and N₂ selectivity, were systematically studied, indicating that the synthesized mesoporous WO₃(1)-CeO₂ has great potential for industrial applications.

© 2016 Elsevier B.V. All rights reserved.

1. Introduction

Recently, release of nitrogen oxides (NO_x) into the air from vehicle exhaust or the burning of coal, diesel fuel, oil, and natural gas has resulted in a variety of serious environmental issues, such as ozone depletion, photochemical smog and acid rain [1–3]. Selective catalytic reduction of NO_x with NH₃ (NH₃-SCR) is an effective technology to reduce NO_x from stationary sources. Based on the reaction temperature window, the SCR process generally contains three types: high-, medium- and low-temperature SCR reactions. The reaction window from 120 to 320 °C usually belongs to the low-temperature region [4]. In thermal power plants and coal-fired boilers, the commercial V₂O₅-WO₃/TiO₂ catalysts have been widely used. However, their working temperature window is too high, which is generally from 300 to 400 °C [5]. Moreover, several inevitable disadvantages of this commercial catalyst restrict its further usages, such as the toxicity of vanadium, weaker sulfur resistance, narrower and higher working temperature window, etc. [6,7]. To overcome these drawbacks, there is an urgent demand to develop novel low-temperature SCR catalysts.

Because of the particular and important structure-activities relationship, mesoporous materials are attracting more attentions recently due to their large specific surface area, highly ordered mesoporous structure and interconnected channels [8,9]. Therefore, there is an increasing trend to apply suitable mesoporous materials in the catalytic field to remove gaseous pollutants such as NO_x. For instance, CeO_x-based mesoporous silica has been used as a catalyst [10]. However, it is easily poisoned by SO₂ or alkali metals, hindering their wider practical application [11–13]. On the other hand, optimal combinations of different metal oxides can usually exhibit better SCR efficiency and thermal stability than single oxides. Li et al. reported that MnO_x-CeO_x can improve the SCR activity, H₂O-resistance and stability by mixing MnO_x with CeO₂ [14–16]. Besides, they usually exhibit many interesting properties in energy conversion and storage, catalysis and adsorption [17,18]. What's more, Ce-W oxides in the NH₃-SCR reaction were studied. For instance, Shan et al. prepared the CeO₂-WO₃ and Ce-W/TiO₂ catalysts and found that the de-NO_x performance and N₂ selectivity were greatly improved by doping W species [19,20]. Chen et al. discovered that the strong interaction between Ce and W is helpful to enhance catalytic activities of NO removal [21]. Peng et al. studied CeO₂-WO₃ bi-metal oxide catalysts, and a mechanism of Ce-W double active center was proposed [22]. However, to the best of our

* Corresponding authors.

E-mail addresses: sihuizhan@nankai.edu.cn (S. Zhan), xli4@utep.edu (X. Li).

knowledge, mesoporous Ce-W oxides catalysts for SCR have never been reported.

In this paper, a series of highly ordered mesoporous $\text{WO}_3(\chi)\text{-CeO}_2$ ($\chi = 0, 0.5, 0.75, 1$ and 1.25) nanomaterials were successfully prepared by using KIT-6 as the hard template. They were further characterized by using TEM, XRD, Raman, BET, $\text{H}_2\text{-TPR}$, $\text{NH}_3\text{-TPD}$, XPS and *in situ* DRIFTS. For investigating its structure-activities relationship, a series of bulk $\text{WO}_3(\chi)\text{-CeO}_2$ ($\chi = 0, 0.5, 0.75, 1$ and 1.25) were prepared to remove NO_x . Using mesoporous $\text{WO}_3(1)\text{-CeO}_2$ as SCR catalyst, 100% NO_x can be cleaned from 225 to 350°C with a gas hourly space velocity (GHSV) of $30\,000\,\text{h}^{-1}$. Besides, several key performance parameters can also be obtained successfully, such as superior water resistance, better alkali metal resistance, higher thermal stability and N_2 selectivity, and so on. In addition, how the novel mesoporous $\text{WO}_3(\chi)\text{-CeO}_2$ nanocomposites affected the $\text{NH}_3\text{-SCR}$ activities at low temperature were also studied and explained in detail based on the systematic characterization.

2. Experimental

2.1. Preparation of materials

In order to prepare the highly ordered mesoporous $\text{WO}_3(1)\text{-CeO}_2$, 3D mesoporous KIT-6 silica was used as a hard template [23]. Typically, $1.2\,\text{g}$ of $(\text{NH}_4)_6\text{W}_7\text{O}_{24}\cdot6\text{H}_2\text{O}$, $1.2\,\text{g}$ of oxalic acid and $1.8\,\text{g}$ of $\text{Ce}(\text{NO}_3)_2\cdot6\text{H}_2\text{O}$ were dissolved in $30\,\text{mL}$ deionized water, and then $1.0\,\text{g}$ of KIT-6 was added to the above mixture. The mixture was stirred overnight at room temperature, dried at 80°C for $4\,\text{h}$ and sintered at 500°C (at a rate of $1\,^\circ\text{C}/\text{min}$ from room temperature) for $4\,\text{h}$ in a muffle furnace. After cooling to room temperature, the obtained powder sample was washed for three times with $2\,\text{M}$ NaOH aqueous solution to remove the silica template, followed by washing with deionized water several times until reaching neutral ($\text{pH}=7$) and then dried at 60°C in an oven.

By the way, the preparation methods of mesoporous $\text{WO}_3(\chi)\text{-CeO}_2$ ($\chi = 0, 0.5, 0.75$ and 1.25) were similar with $\text{WO}_3(1)\text{-CeO}_2$ by varying the doped ratio of $(\text{NH}_4)_6\text{W}_7\text{O}_{24}\cdot6\text{H}_2\text{O}$. What's more, the preparation processes of bulk $\text{WO}_3(\chi)\text{-CeO}_2$ were similar with mesoporous $\text{WO}_3(\chi)\text{-CeO}_2$, except that no KIT-6 was added into the mixture during the bulk $\text{WO}_3(\chi)\text{-CeO}_2$ preparation. $0.3\,\text{K}/\text{WO}_3(1)\text{-CeO}_2$ was prepared by a conventional impregnation method. The fresh catalyst was added to $0.30\,\text{wt\%}$ potassium nitrate solution. After the mixed solution was stirred to dry at 60°C , and then calcined at 500°C for $4\,\text{h}$. The $\text{V}_2\text{O}_5\text{-WO}_3/\text{TiO}_2$ catalyst used in the experiment was commercial honeycomb-like $\text{V}_2\text{O}_5\text{-WO}_3/\text{TiO}_2$ catalyst, which was used without further purification.

2.2. Characterization

The morphology and structure of mesoporous $\text{WO}_3(\chi)\text{-CeO}_2$ were measured by transmission electron microscopy (TEM) with a JEOL Model JEM-2100F at $200\,\text{kV}$. The X-ray diffraction (XRD) patterns were carried out by using an X-ray diffractometer apparatus (Rigaku D/Max 2200PC, $\lambda = 0.15418\,\text{nm}$) with the voltage and electric current of $40\,\text{kV}$ and $40\,\text{mA}$. The N_2 adsorption-desorption isotherms were measured by using the Quantachrome AutoSorb iQ-MP operated at -196°C . The specific surface area was measured by using the Brunauer-Emmett-Teller (BET) method, and the pore size distributions of samples were recorded with BJH method. Temperature-programmed reduction of hydrogen ($\text{H}_2\text{-TPR}$) and temperature-programmed desorption of NH_3 ($\text{NH}_3\text{-TPD}$) were measured by a Micromeritics Autochem 2920 II apparatus with the thermal conductivity detector (TCD) [24]. And *in situ* Diffuse Reflectance Infrared Fourier Transform spectra (*in situ* DRIFTS) were acquired using the Nicolet iS50 spectrometer. Prior to each

experiment, the samples were heated to 300°C in an N_2 atmosphere for $2\,\text{h}$ and then cooled to the desired temperature.

2.3. Catalytic activity test

The $\text{NH}_3\text{-SCR}$ activities were measured in a fixed-bed quartz reactor with $10\,\text{mm}$ inner diameter under atmospheric pressure from 100°C to 400°C . The typical inlet gas component was $500\,\text{ppm}$ NO and $500\,\text{ppm}$ NH_3 , $5\,\text{vol\%}$ O_2 , N_2 balance, $10\,\text{ol\%}$ or $15\,\text{vol\%}$ H_2O (when used), $100\,\text{ppm}$ SO_2 (when needed). The total flow rate of feeding gases was $200\,\text{mL}/\text{min}$, with a gas hourly space velocity (GHSV) of $30,000\,\text{h}^{-1}$. Before the test, $0.5\,\text{g}$ sample was pressed into blocks, then crushed and sieved with $40\text{--}60$ meshes. And the component and concentration of outlet gas were measured by KM-940 flue gas analyzer (Kane International Limited, UK). The NO_x conversion ratio and N_2 selectivity were calculated by the following equations:

$$\text{NO}_x \text{ conversion (\%)} = \frac{[\text{NO}_x]_{\text{in}} - [\text{NO}_x]_{\text{out}}}{[\text{NO}_x]_{\text{in}}} \times 100\%$$

$$\text{N}_2 \text{ selectivity (\%)} = \left(1 - \frac{2[\text{N}_2\text{O}]_{\text{out}}}{[\text{NO}_x]_{\text{in}} + [\text{NH}_3]_{\text{in}} - [\text{NO}_x]_{\text{out}} - [\text{NH}_3]_{\text{out}}} \right) \times 100\%$$

Herein NO_x included NO and NO_2 , where the $[\text{NO}_x]_{\text{in}}$ and $[\text{NO}_x]_{\text{out}}$ indicated the inlet and outlet concentration at steady-state, respectively.

3. Results and discussion

3.1. Materials characterization

3.1.1. TEM analysis

In order to explore microstructure of mesoporous $\text{WO}_3(1)\text{-CeO}_2$, the typical TEM tests were conducted and the results were shown in Fig. 1. From Fig. 1a, it could conclude that the sample was highly ordered mesoporous structure. Moreover, it was found that the average pore diameter of mesoporous $\text{WO}_3(1)\text{-CeO}_2$ was $2.9\,\text{nm}$ (Fig. 1b), which was similar with $3.6\,\text{nm}$ wall thickness of KIT-6 (Fig. S1e), suggesting that cubic mesoporous $\text{WO}_3(1)\text{-CeO}_2$ was replicated successfully by thermal decomposition of metal precursors within the restricted channels of KIT-6 [25]. In Fig. 1c, lattice fringe ($d = 0.28\,\text{nm}$) belonged to the (100) crystallographic planes of CeO_2 , and the (110) crystallographic planes ($d = 0.31\,\text{nm}$) were observed clearly [26,27]. The lattice fringe of WO_3 belonging to the (020) crystallographic planes ($d = 0.375\,\text{nm}$) was also observed [28], indicating that it was well crystallized. With increasing W-doping ratio, the mesoporous channels became not obvious (Fig. S1). In addition, X-ray energy dispersive spectroscopy (EDS) was performed to investigate the chemical composition of mesoporous $\text{WO}_3(1)\text{-CeO}_2$ and the results confirmed that the sample was composed of Ce, W and O elements (Fig. 1d).

3.1.2. BET analysis

To further investigate the surface areas of mesoporous $\text{WO}_3(\chi)\text{-CeO}_2$, we characterized the catalysts using BET analysis. The N_2 adsorption-desorption isotherms and the pore diameter distribution of mesoporous CeO_2 , $\text{WO}_3(0.5)\text{-CeO}_2$, $\text{WO}_3(0.75)\text{-CeO}_2$, $\text{WO}_3(1)\text{-CeO}_2$, $\text{WO}_3(1.25)\text{-CeO}_2$ and bulk WO_3 were evaluated and listed in Table 1. Fig. 2a suggested that the adsorption-desorption curves of mesoporous CeO_2 and $\text{WO}_3(\chi)\text{-CeO}_2$ can be classified as type IV isotherms in the relative pressure from 0.6 to 0.95 . All the isotherms were very similar, with a type H1 hysteresis loop [22], indicating that these structures possessed highly ordered mesoporous channels, which were in accordant with TEM results. As

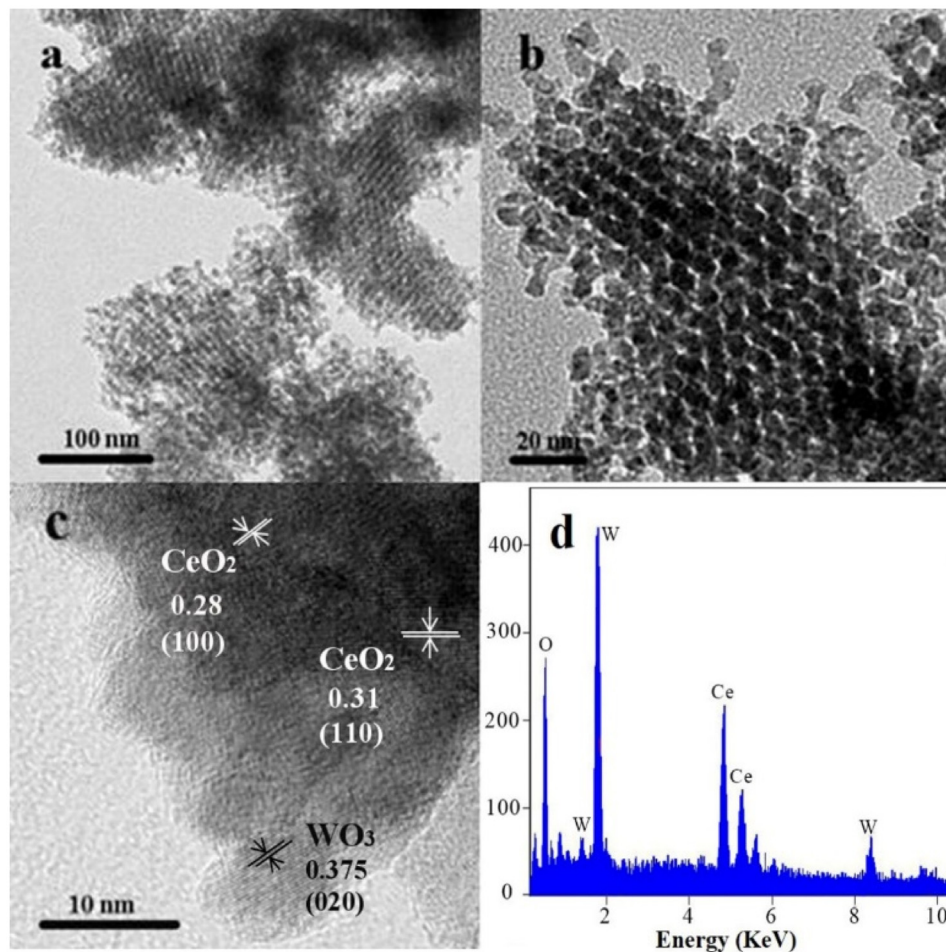


Fig. 1. (a, b) TEM images, (c) HRTEM and (d) energy spectrum analysis (EDS) images of mesoporous WO₃(1)-CeO₂.

Table 1

Summary of textural parameters of the samples.

Materials	Specific area (m ² /g)	Pore volume (cc/g)	Pore diameter (nm)
Mesoporous CeO ₂	163.3	0.46	3.41
Mesoporous WO ₃ (0.5)-CeO ₂	91.1	0.28	2.46
Mesoporous WO ₃ (0.75)-CeO ₂	105.6	0.27	2.22
Mesoporous WO ₃ (1)-CeO ₂	100.2	0.26	2.02
Mesoporous WO ₃ (1.25)-CeO ₂	89.4	0.25	2.11
Bulk WO ₃	5.3	0.02	15.76

depicted in Fig. 2b, the average pore sizes of these mesoporous materials were mainly focused on 3.2 nm, indicating that the pore size distribution of all the samples was uniform relatively. However, there was no typical adsorption-desorption curve for bulk WO₃ catalysts, suggesting that the sample had no ordered pore structure. According to Fig. 2b, the average pore size of bulk WO₃ was much bigger than other mesoporous catalysts. Considering the low specific area (5.3 m²/g) and small pore volume (0.02 cc/g) of bulk WO₃ (Table 1), it can be assumed that the bulk WO₃ was made up of sintered particles. The results suggested that the mesoporous structure can effectively inhibit the crystallization of the catalyst.

As shown in Table 1, it was found that the surface area of mesoporous CeO₂ was 163.3 m²/g, which was larger comparing to those of mesoporous WO₃(0.5)-CeO₂ (91.1 m²/g), WO₃(1)-CeO₂ (100.2 m²/g) and mesoporous WO₃(1.25)-CeO₂ (89.4 m²/g). Because pure metal oxide was easier to form mesoporous structure, and the regularity property of mesoporous CeO₂ was better than mesoporous WO₃(χ)-CeO₂ (χ = 0.5, 0.75, 1, 1.25), which was

in agreement with the result of TEM analysis. Also, the pore volume and pore diameter became smaller gradually with the increase of W-doping ratio, which was due to the increased tungsten content damaging the pore channel and making the formation of pore structure less likely.

3.1.3. XRD patterns

To further study their microstructure, low-angle XRD patterns of mesoporous WO₃(χ)-CeO₂ were analyzed and the results were shown in Fig. 3a. The stronger diffraction peaks of (211) plane around 1.2° for mesoporous WO₃(χ)-CeO₂ were observed, suggesting that the ordered mesoporous structure came into being [29]. Furthermore, with increasing W-doping content, the intensity of diffraction peaks became weaker and weaker, and the peak positions also shifted to a higher-angle region, indicating that parts of mesoporous channels collapsed. It was demonstrated that the regularity of mesoporous samples was much poorer than pure mesoporous CeO₂, which may be due to the doped tungsten result-

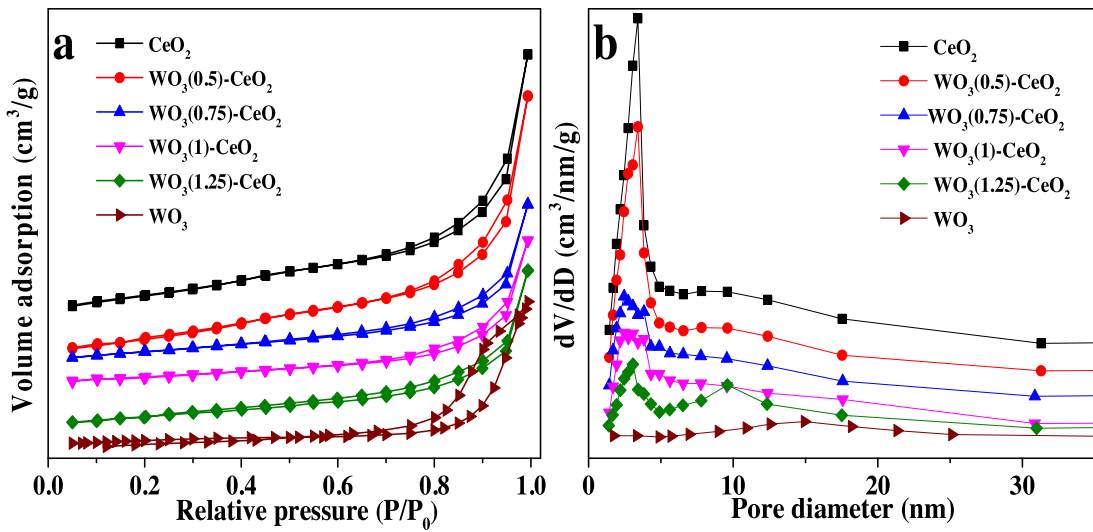


Fig. 2. (a) N_2 adsorption-desorption isotherms, (b) pore diameter distribution.

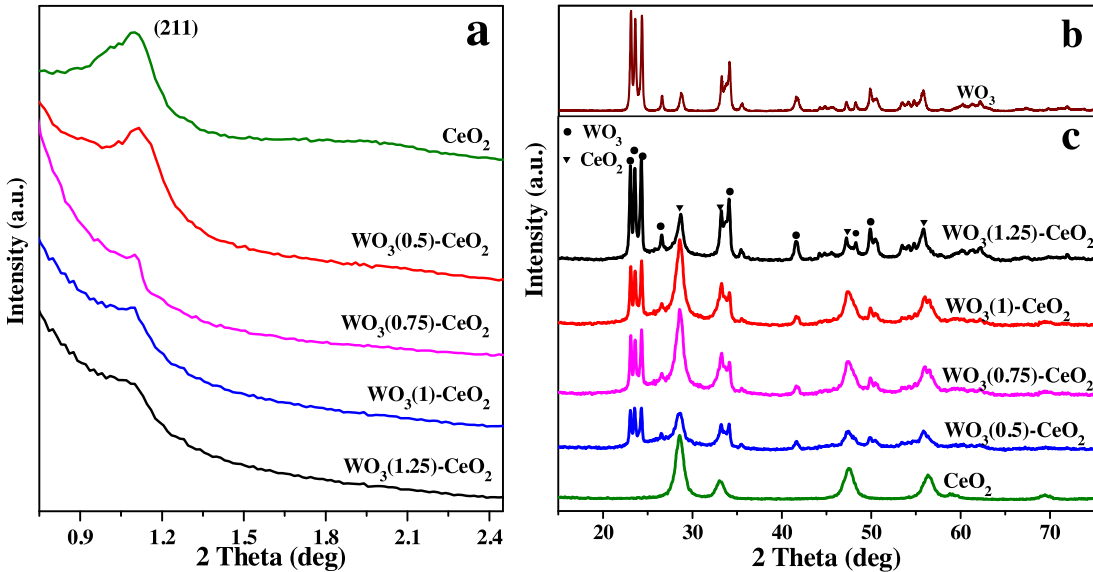


Fig. 3. (a) Low-angle XRD; (b) wide-angle XRD patterns of bulk WO_3 ; (c) wide-angle XRD patterns of mesoporous $\text{WO}_3(\chi)\text{-CeO}_2$.

ing in channel collapse. It can also be verified from BET analysis results [30,31]. Moreover, it was difficult to prepare pure mesoporous WO_3 , indicating that tungsten element had a devastating impact on the formation of mesoporous channels.

Furthermore, wide-angle XRD patterns of bulk WO_3 and mesoporous $\text{WO}_3(\chi)\text{-CeO}_2$ results were depicted in Fig. 3b and c. The spectrum of bulk WO_3 was individually presented in Fig. 3b because of its strong intensity that can make weaker peaks unobvious if the spectra of all the catalysts were put together. As shown in Fig. 3b, the diffraction peaks of bulk WO_3 were well indexed to WO_3 (JCPDS20-1324). In Fig. 3c, compared with pure mesoporous CeO_2 , the diffraction peaks of WO_3 could be verified and the peak intensity became stronger with increasing W-doping ratio. And the diffraction peaks of mesoporous $\text{WO}_3(\chi)\text{-CeO}_2$ can be well indexed to CeO_2 (JCPDS 81-0792) [15] and WO_3 (JCPDS20-1324) [30]. Furthermore, no peaks of other crystal phases were detected, indicating that the prepared mesoporous $\text{WO}_3(\chi)\text{-CeO}_2$ catalysts were made up of CeO_2 and WO_3 . In addition, the average particle sizes of WO_3 and CeO_2 in mesoporous $\text{WO}_3(1)\text{-CeO}_2$ were calcu-

lated to be about 8 nm and 7 nm based on the Scherrer formula, which were in agreement with 5.44 nm from TEM.

3.1.4. Raman characterization

Raman spectrum (Fig. 4) was employed to further characterize the existence states of the tungsten species (WO_x) in the mixed Ce-W bi-metal oxides catalysts. The spectrum of CeO_2 showed a sharp peak at 461 cm^{-1} , which belonged to the F_{2g} mode of the symmetric breathing mode of oxygen atoms surrounding cerium ions in the cubic fluorite phase CeO_2 [32]. As for $\text{WO}_3(\chi)\text{-CeO}_2$ catalysts, the peak that belonged to the F_{2g} mode of CeO_2 became weaker significantly. At the same time, the peaks at $900\text{--}1000 \text{ cm}^{-1}$ enhanced gradually, suggesting that the adding of tungsten species inhibited the crystallization of CeO_2 . The conclusion was highly consistent with the XRD results. However, it's worth mentioning that the Ce-O vibration peak shifted to much lower wavenumber, which may be related with the decreased CeO_2 particle size [33]. Also, typical WO_3 crystallization peaks (272, 716 and 806) occurred on the $\text{WO}_3(\chi)\text{-CeO}_2$ and WO_3 catalysts [34]. Through the analysis, we could realize that the $\text{WO}_3(\chi)\text{-CeO}_2$ catalysts remained the cubic

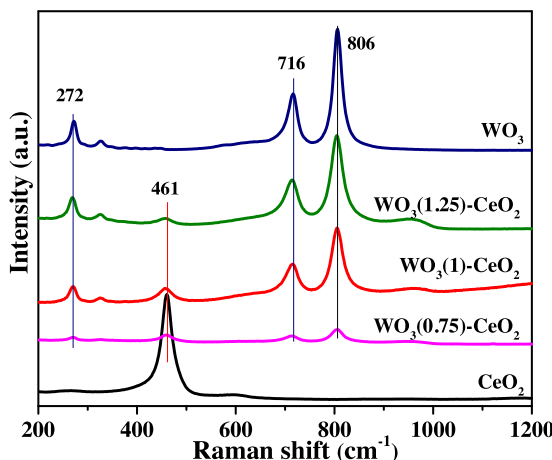


Fig. 4. Raman patterns of mesoporous $\text{WO}_3(\chi)\text{-CeO}_2$ and WO_3 .

fluorite structure of CeO_2 and the tungsten species existed mainly in the state of crystalline WO_3 .

3.1.5. $\text{NH}_3\text{-TPD}$

To better analyze the different acidic sites and their relative strength on the surface of the materials, $\text{NH}_3\text{-TPD}$ patterns of mesoporous $\text{WO}_3(\chi)\text{-CeO}_2$ with different W-doping ratio were measured (Fig. 5a). Because the thermal stability of the NH_4^+ restrained in the Brønsted acid sites was lower than the NH_3 molecules attributed to the Lewis acid sites, it can be concluded that the desorption peaks at high temperatures originated from the Lewis acid sites, and the peaks below 200 °C belonged to Brønsted acid sites [35]. Moreover, the temperature window of Lewis acid sites was wider than Brønsted acid sites. Additionally, there was a stronger peak around 132 °C for mesoporous CeO_2 , which belonged to NH_4^+ ions resulting from Brønsted acid sites. Two obvious peaks resulted from the coordinated NH_3 molecules appeared from 250 to 450 °C, which belonged to the Lewis acid sites [36,37]. However, for mesoporous $\text{WO}_3(\chi)\text{-CeO}_2$ ($\chi = 0.5, 0.75, 1, 1.25$), their desorption peaks shifted to higher temperatures. And the peak intensity became stronger compared with pure mesoporous CeO_2 and pure WO_3 , which may be due to the synergistic effect between tungsten and cerium oxides. What's more, the amount of peaks above 300 °C increased, which were associated with coordinated NH_3 molecules originating from Lewis acid sites at high temperatures. It can also be proved by the desorption curve of pure WO_3 , which only owned the obvious peak at 200 °C related to Brønsted acid sites. For mesoporous $\text{WO}_3(0.75)\text{-CeO}_2$, two NH_3 desorption peaks at 531 and 590 °C were due to weakly bonded and strongly bonded NH_3 , respectively, which were related to Lewis acid sites [9]. Meanwhile, it was reported that NH_3 adsorbed species could be more easily desorbed due to the addition of tungsten element at higher temperature [37]. Furthermore, the $\text{NH}_3\text{-TPD}$ curve of mesoporous $\text{WO}_3(1)\text{-CeO}_2$ showed larger area than other samples at high temperatures, indicating that there were enough Lewis acid sites on the surface. It was well known that the amount of the Lewis acid sites played a significant role in $\text{NH}_3\text{-SCR}$ activity [22], and more Lewis acid sites on the surface of mesoporous $\text{WO}_3(1)\text{-CeO}_2$ resulted in preferable removal efficiency at the low temperature region.

3.1.6. Reducibility ($\text{H}_2\text{-TPR}$)

As we all know, the surface reduction ability of materials played an important role in $\text{NH}_3\text{-SCR}$ activity. The $\text{H}_2\text{-TPR}$ test of mesoporous $\text{WO}_3(\chi)\text{-CeO}_2$ was shown in Fig. 5b, which presented that the reduction potentials of mesoporous $\text{WO}_3(\chi)\text{-CeO}_2$ were weaker than mesoporous CeO_2 below 500 °C. For mesoporous CeO_2 , the

reduction peak at 450 °C could be attributed to the reduction of surface oxygen species [38]. It was found that the reduction peaks of the bulk oxygen (bulk Ce^{4+} to Ce^{3+}) and the surface oxygen (surface Ce^{4+} to Ce^{3+}) of ceria focused on 650 and 508 °C, respectively [39]. Comparing with mesoporous CeO_2 , the peak of mesoporous $\text{WO}_3(1)\text{-CeO}_2$ at 550 and 740 °C could be attributed to the reduction of surface oxygen species because of the oxygen vacancies in Ce-W composite. For pure WO_3 , the three peaks at 600, 698, 788 °C can be ascribed to the stepwise reduction of tungsten from W^{6+} to W^0 [15,21]. Comparing with mesoporous CeO_2 and pure WO_3 , the peak of mesoporous $\text{WO}_3(\chi)\text{-CeO}_2$ ($\chi = 0.5, 0.75, 1, 1.25$) assigning to the transformation of tungsten shifted to lower temperatures, which would be favorable to improve $\text{NH}_3\text{-SCR}$ activity.

3.1.7. XPS analysis

The XPS spectra of Ce 3d, O 1s and W 4f on mesoporous $\text{WO}_3(\chi)\text{-CeO}_2$ were shown in Fig. 6, these kinds of absorbed peaks were calibrated against the C 1s peak standardized at 284.6 eV [40]. As shown in Fig. 6a, Ce 3d, O 1s and W 4f appeared in the survey spectrum XPS spectra for mesoporous $\text{WO}_3(\chi)\text{-CeO}_2$. The XPS spectra of chemical states of Ce over different materials were showed in Fig. 6b. The peaks assigned u1 and v1 were the main representatives of the $3d^{10}4f^1$ electronic state of Ce^{3+} ions, while the peaks assigned u, u2, u3, v, v2 and v3 were the representative of the $3d^{10}4f^0$ state corresponding to Ce^{4+} [37]. The amount of Ce^{3+} increased gradually from 15.8% to 22.49% by the W-doping. The increasing amount of Ce^{3+} was due to the interaction between cerium and the neighboring atoms such as W. The existence of the Ce^{3+} species could bring about a charge imbalance and unsaturated chemical bonds on the sample surface, thereby resulting in the improvement of chemisorbed oxygen on the surface [24,41]. The increase of chemisorbed oxygen was beneficial to SCR reaction.

As presented in Fig. 6c, two kinds of surface oxygen species were identified by performing a peak-fitting deconvolution. The peaks at higher Binding Energy of 531.0–533.0 eV were assigned to the surface chemisorbed oxygen (O_α), and the peaks at lower Binding Energy of 529.0–531.0 eV were attributed to the surface lattice oxygen (O_β). The ratio of $\text{O}_\alpha/(\text{O}_\alpha+\text{O}_\beta)$ in mesoporous CeO_2 (27.5%) was much lower than that in mesoporous $\text{WO}_3(1)\text{-CeO}_2$ (39.8%), which may be due to the interaction between the tungsten and cerium oxides with the W-doping. It is well known that the higher rate of O_α would have significant promotion of the SCR activity, which was proved by the following SCR catalytic test results.

The W4f spectra of the tungsten-containing catalysts were shown in Fig. 6d. With increasing tungsten content, the peak position of these five catalysts had no significant change, suggesting that neighboring environment of the W^{6+} cations stayed the same to a certain extent [22,23]. However, it's worth noting that peak intensities enhanced gradually with the increasing of WO_3 concentration. The enhancement of the peak intensity suggested the increase of the tungsten molar density on the surface. And the above characteristics were in consistent with the analysis results of $\text{H}_2\text{-TPR}$ as well.

3.2. The $\text{NH}_3\text{-SCR}$ activity

The $\text{NH}_3\text{-SCR}$ activity measurements of mesoporous $\text{WO}_3(\chi)\text{-CeO}_2$ and bulk WO_3 materials were presented in Fig. 7a. It shows that 100% NO_x conversion ratio with mesoporous $\text{WO}_3(1)\text{-CeO}_2$ can be reached from 225 to 350 °C with a GHSV of 30 000 h⁻¹, which may be due to the stronger synergistic effect of WO_3 and CeO_2 and more adsorbed NO_x and NH_3 species. The decrement of NO_x conversion at high temperature was basically due to the emergence of the NH_3 oxidation phenomenon. (see Fig. S4 for details of the NH_3 oxidation analysis). However, when an excess amount of W was added, the NO_x conversion ratio would decrease, which

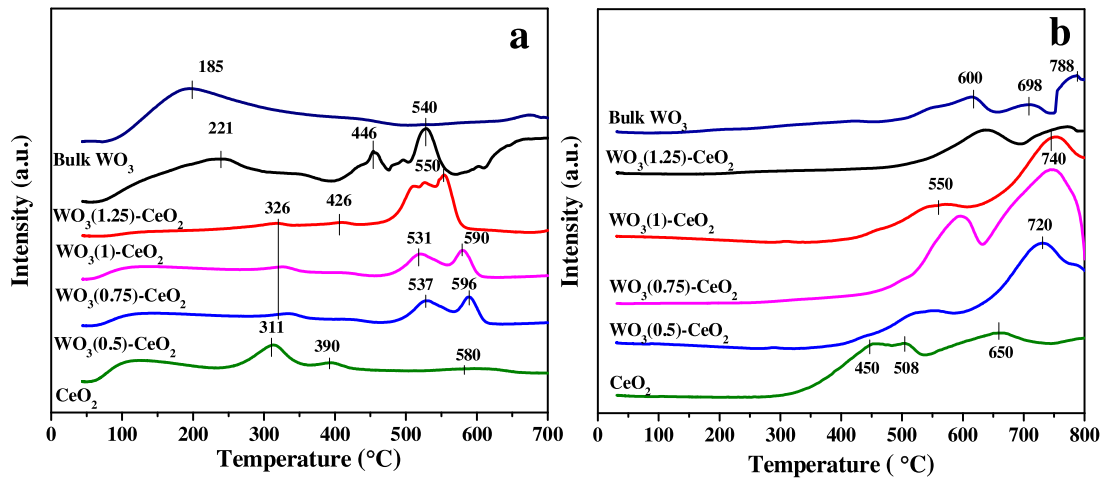


Fig. 5. (a) NH₃-TPD and (b) H₂-TPR patterns of mesoporous WO₃(χ)-CeO₂ and bulk WO₃.

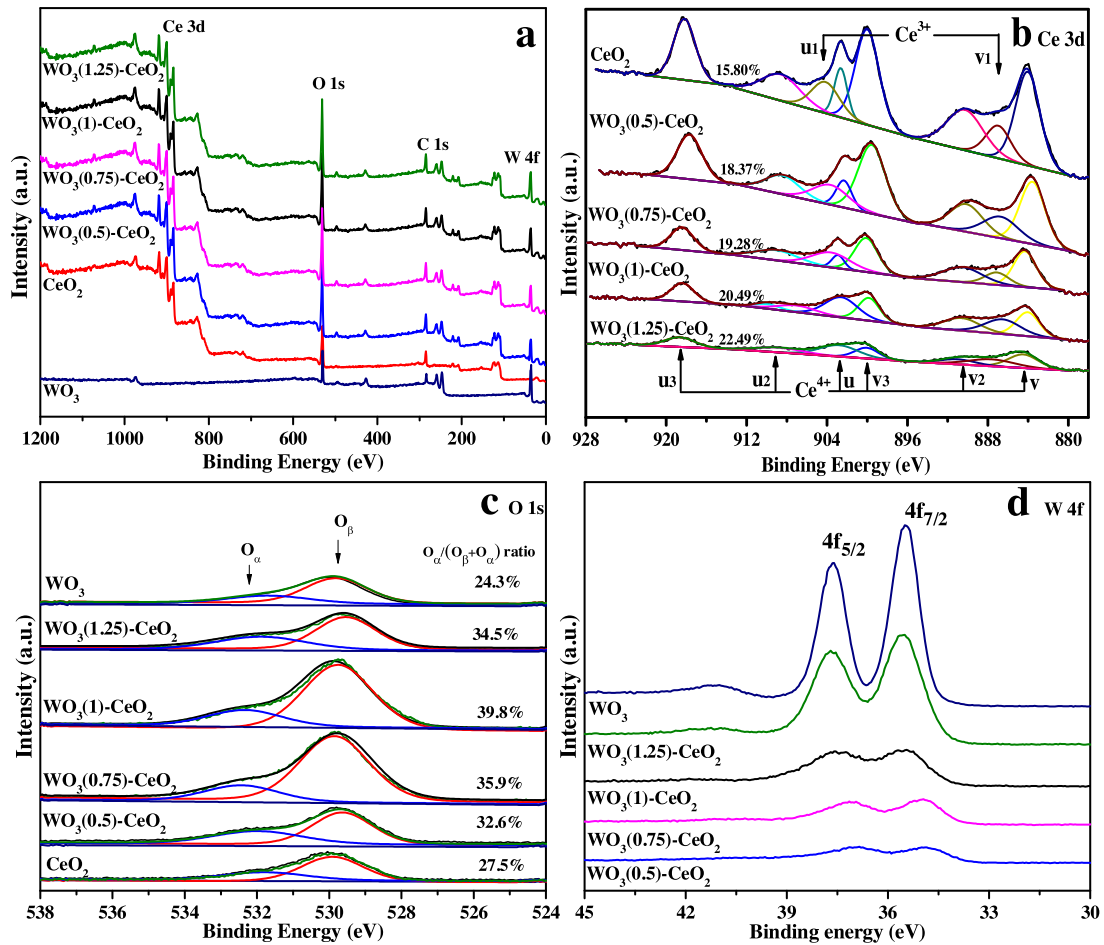


Fig. 6. XPS spectrum of mesoporous WO₃(χ)-CeO₂, (a) wide-scan spectra, (b) Ce 3d, (c) O 1s, (d) W 4f.

showed that the optimal doping ratio was 1:1. Furthermore, the NH₃-SCR activity of mesoporous WO₃(1)-CeO₂ was better than other mesoporous WO₃(χ)-CeO₂ (χ =0.5, 0.75, 1.25) catalysts at lower temperatures from 100 to 225 °C. The NO_x conversion ratio of mesoporous WO₃(1)-CeO₂ was better than bulk (non-mesoporous) WO₃(1)-CeO₂ and commercial V₂O₅-WO₃/TiO₂ catalysts from 100 to 300 °C, which may be related to the unique structure-activity relationship of the mesoporous structure (Fig. 7b). The NO_x con-

version ratios of bulk WO₃(χ)-CeO₂ and bulk pure WO₃ were presented in Supporting information (Fig. S3).

3.3. The effect of H₂O, alkali metal poisoning, SO₂ resistance and thermal stability

As we all know, water vapor from NH₃-SCR reaction process may affect the NO_x conversion ratio. Therefore, it is necessary to determine how the water vapor affected their SCR activities. In

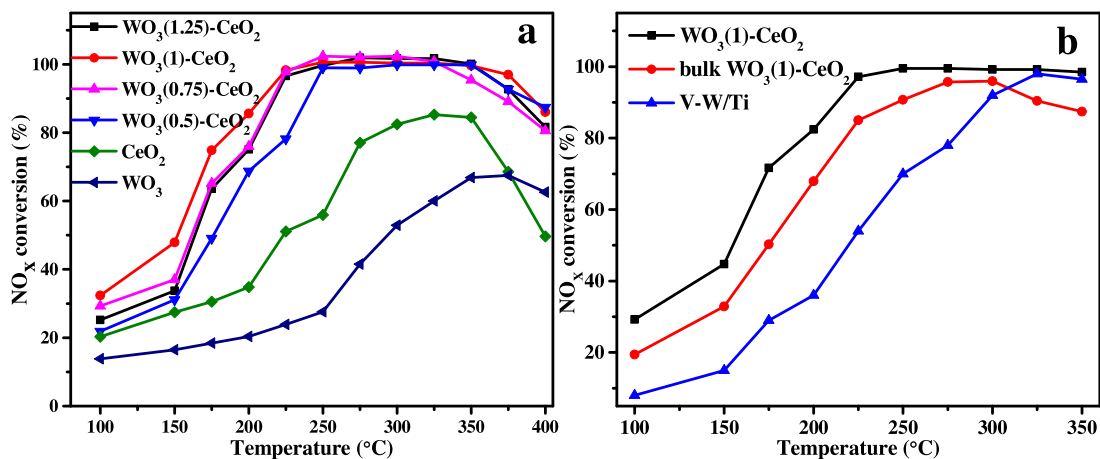


Fig. 7. NO_x conversion ratio of (a) mesoporous WO₃(χ)-CeO₂ and bulk WO₃, and (b) different kind of SCR catalysts under 500 ppm NO, 500 ppm NH₃, 5% O₂, GHSV of 30 000 h⁻¹ and N₂ balance gas.

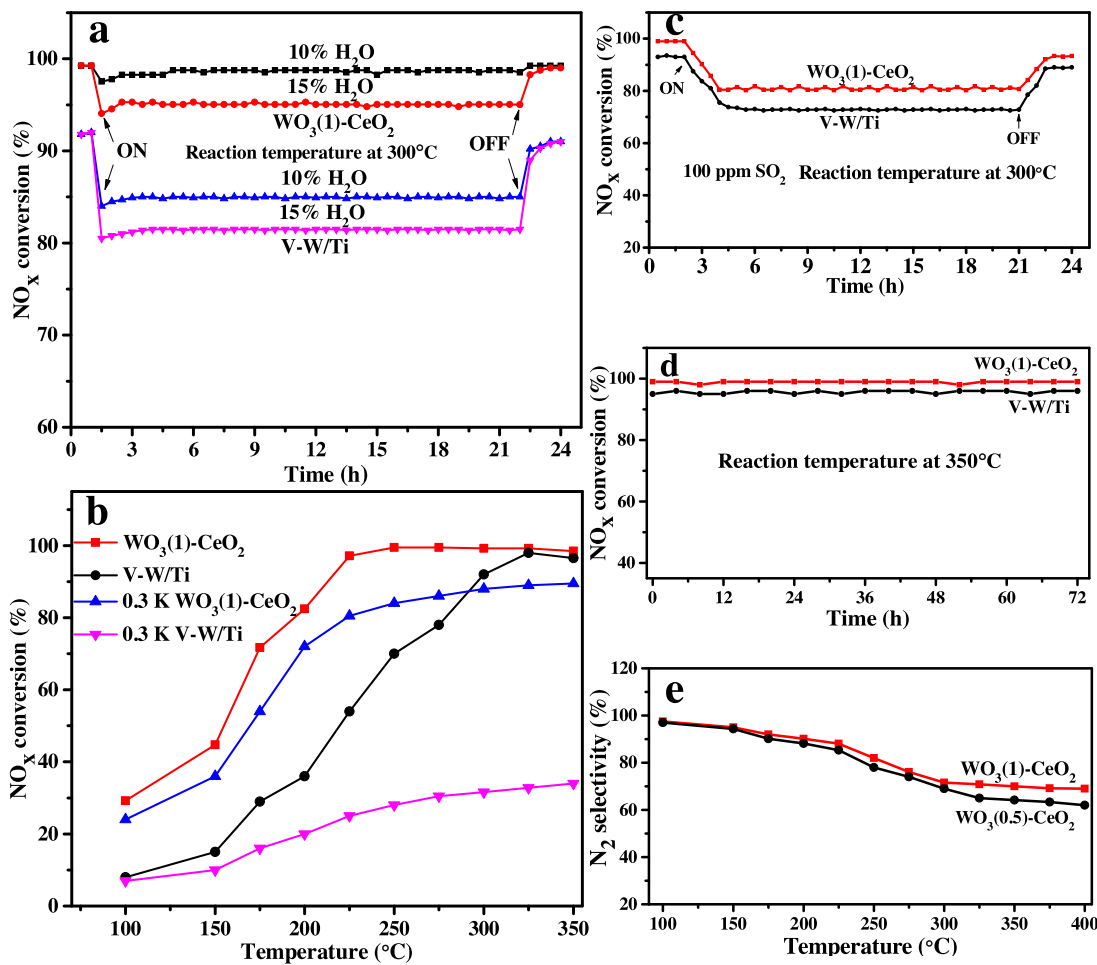


Fig. 8. NH₃-SCR activity of the mesoporous WO₃(1)-CeO₂ and commercial V₂O₅-WO₃/TiO₂: (a) H₂O resistance, (b) resistance of alkali metal, (c) SO₂ tolerance, (d) stability test and (e) N₂ selectivity. Reaction conditions: [NO] = [NH₃] = 500 ppm, [O₂] = 5 vol%, [H₂O] = 10% or 15% (when used), [SO₂] = 100 ppm (when used), N₂ balance and GHSV = 30 000 h⁻¹.

order to explore the effect of water vapor, 10% or 15% H₂O was added into the system with GHSV of 30 000 h⁻¹ at 300 °C (Fig. 8a). It was found that the NO_x conversion ratio of mesoporous WO₃(1)-CeO₂ and commercial V₂O₅-WO₃/TiO₂ at 300 °C was 100% and 91%, respectively. Under 10% or 15% H₂O, NO_x conversion ratio of mesoporous WO₃(1)-CeO₂ declined to 98% and 95%, respectively. In contrast, the conversion ratio of V₂O₅-WO₃/TiO₂ decreased to

84% and 81%, respectively, which was caused by the blocked active sites on the catalyst surface. Furthermore, it was found that the NO_x conversion ratio decreased with increasing water content, indicating that the presence of water vapor had an obvious influence on the active sites of samples. The negative effect of H₂O was more serious for commercial V₂O₅-WO₃/TiO₂ than mesoporous samples. After turning off the H₂O entrance, the NO_x conversion ratio of

mesoporous $\text{WO}_3(1)\text{-CeO}_2$ could recover to 100% soon, but commercial $\text{V}_2\text{O}_5\text{-WO}_3/\text{TiO}_2$ could recover only 90%. Therefore, these mesoporous materials have better water tolerance. Meanwhile, it was suggested that the effect of H_2O on $\text{NH}_3\text{-SCR}$ activity with mesoporous $\text{WO}_3(1)\text{-CeO}_2$ was reversible.

The $\text{NH}_3\text{-SCR}$ activity measurements of mesoporous $\text{WO}_3(1)\text{-CeO}_2$, commercial $\text{V}_2\text{O}_5\text{-WO}_3/\text{TiO}_2$ catalyst and homologous 0.3 wt% K-doped samples at 100–400 °C were presented in Fig. 8b [15]. For $\text{V}_2\text{O}_5\text{-WO}_3/\text{TiO}_2$ catalyst with 0.3 wt% K-doping, the activity decreased significantly, only producing 35% NO_x conversion ratio. For 0.3 wt% K-doped mesoporous $\text{WO}_3(1)\text{-CeO}_2$, although the NO_x conversion ratio was lower compared to the fresh, it could also reach 76% at 225 °C during the test. Therefore, it was proved that the novel mesoporous $\text{WO}_3(1)\text{-CeO}_2$ can provide much stronger alkali resistance than commercial $\text{V}_2\text{O}_5\text{-WO}_3/\text{TiO}_2$ catalyst. According to previous reports, the decreases in the reducibility and the surface acidity should be responsible for the alkali metal poisoning of the catalysts [15,41].

The SO_2 tolerance tests for mesoporous $\text{WO}_3(1)\text{-CeO}_2$ and commercial $\text{V}_2\text{O}_5\text{-WO}_3/\text{TiO}_2$ were also shown in Fig. 8c. After pumping into SO_2 , the NO_x conversion ratio of mesoporous $\text{WO}_3(1)\text{-CeO}_2$ decreased from 100% to 81%. As for commercial $\text{V}_2\text{O}_5\text{-WO}_3/\text{TiO}_2$, there was 73% removal efficient. The sulfur-poisoning of catalysts may be caused by the formation of thermally stable sulfate species, which deposited on catalysts' surface and blocked catalytic sites [42,43]. However, after cutting off inlet SO_2 , the NO_x conversion ratio of mesoporous $\text{WO}_3(1)\text{-CeO}_2$ recovered to 93% after 3 h, and remained at 93%, showing that the mesoporous $\text{WO}_3(1)\text{-CeO}_2$ had better reversible inhibition effect.

The thermal stability of mesoporous $\text{WO}_3(1)\text{-CeO}_2$ and commercial $\text{V}_2\text{O}_5\text{-WO}_3/\text{TiO}_2$ catalyst were presented in Fig. 8d. The NO_x conversion ratio of mesoporous $\text{WO}_3(1)\text{-CeO}_2$ and commercial $\text{V}_2\text{O}_5\text{-WO}_3/\text{TiO}_2$ maintained at 100% and 91% at 300 °C for 72 h, respectively. It showed that the aging ability of sample was just as good as $\text{V}_2\text{O}_5\text{-WO}_3/\text{TiO}_2$ catalyst, which was a very important factor in practical application. Also, the N_2 selectivity test was shown in Fig. 8e and our test results showed that the $\text{WO}_3(1)\text{-CeO}_2$ catalyst had a relatively high N_2 selectivity under low temperature, while the N_2 selectivity became lower under higher temperature, which may be due to the increasing intermediate product (NH_4NO_3) in the $\text{NH}_3\text{-SCR}$ reaction, resulting in lower N_2 selectivity at high temperatures [22]. Moreover, the N_2 selectivity of mesoporous $\text{WO}_3(1)\text{-CeO}_2$ was better than mesoporous $\text{WO}_3(0.5)\text{-CeO}_2$, proving that the higher N_2 selectivity could be conducive to promote the excellent NH_3 oxidation ability.

3.4. In situ DRIFTS

3.4.1. NH_3 adsorption

The *in situ* DRIFT spectra were carried out and the results were shown in Fig. 9. Prior to the experiment of gas adsorption, the mesoporous CeO_2 , $\text{WO}_3(1)\text{-CeO}_2$ and bulk $\text{WO}_3(1)\text{-CeO}_2$ were firstly treated with N_2 for 2 h at 300 °C to blow away the CO_2 and H_2O in air, and then measured the background spectra under the same conditions. When cooling to the goal temperature of 50 °C, 500 ppm NH_3 was pumped into the system for 30 min, and then the *in situ* DRIFT spectra were measured with the increasing temperature. The recorded results were presented in Figs. 9 a and S6 (a, c). For mesoporous $\text{WO}_3(1)\text{-CeO}_2$, the peak at 1402 cm⁻¹ was correlated to NH_4^+ ions, and the peak at 1592 cm⁻¹ was assigned to the coordinated NH_3 linked to Lewis acid sites [44]. The peaks at 1232 and 1543 cm⁻¹ may be resulted from the metabolic species of adsorbed ammonia species from Lewis acid sites [44,45]. The peak at 1102 cm⁻¹ was assigned to symmetric deformation of harmonious NH_3 . A new peak at 1358 cm⁻¹ for mesoporous $\text{WO}_3(1)\text{-CeO}_2$ was quite different from adsorbed NH_3 and NO_x species, which may

be attributed to the formed intermediate species during $\text{NH}_3\text{-SCR}$ reaction. It was obvious that Brønsted acid sites and Lewis acid sites coexisted on the samples surface, suggesting that NH_3 could be adsorbed on different active sites. Compared with Fig. S6 (a, c), Fig. 9a showed that both the addition of tungsten oxides to CeO_2 and the mesoporous structure would result in more NH_3 adsorption sites, which was significantly beneficial to $\text{NH}_3\text{-SCR}$ reaction. It was in good consistent with the result of $\text{NH}_3\text{-TPD}$ analysis.

3.4.2. $\text{NO} + \text{O}_2$ adsorption

The *in situ* DRIFT spectra of $\text{NO} + \text{O}_2$ adsorption were presented in Figs. 9 b and S6(b, d). Several peaks in the range of 1000–2000 cm⁻¹ were detected. The peaks of mesoporous $\text{WO}_3(1)\text{-CeO}_2$ were stronger than mesoporous CeO_2 (Fig. S6b), which may connect with the synergistic effect between the tungsten and cerium species. The peaks at 1095 and 1193 cm⁻¹ belonged to asymmetric and symmetric NO_2 vibration of monodentate nitrite, respectively [44]. The peaks at 1545, and 1246 cm⁻¹ were due to asymmetric and symmetric NO_2 vibration of bidentate nitrate, respectively [46]. The band at 1605 cm⁻¹ was assigned to bridging nitrate, which originated from the adsorbed NO_2 on the oxide surface. For mesoporous $\text{WO}_3(1)\text{-CeO}_2$, the peak at 1193 cm⁻¹ moved to 1246 cm⁻¹ with temperature increasing, suggesting that the surface species transformed from monodentate nitrite to bidentate nitrate. Compared with Fig. S6 (b, d), Fig. 9b indicated that the mesoporous structure and the synergistic effect between cerium oxide and tungsten oxide species were beneficial to the formation of monodentate nitrate, bidentate nitrate and bridging nitrate species. More monodentate nitrite species, bidentate nitrate and bridging nitrate species on the surface of mesoporous $\text{WO}_3(1)\text{-CeO}_2$ were necessary to improve the $\text{NH}_3\text{-SCR}$ activity.

3.4.3. Reactions between NH_3 and adsorbed $\text{NO} + \text{O}_2$ species

In order to explore the reactivity of adsorbed NO_x species in the SCR reaction on mesoporous $\text{WO}_3(1)\text{-CeO}_2$ surface, *in situ* DRIFTS of the reaction between preadsorbed NO_x and NH_3 at 200 °C was tested and the results were shown in Fig. 9c. After the adsorption of $\text{NO} + \text{O}_2$, the surface of the material was mainly covered by bridging nitrate (at 1581 cm⁻¹) and bidentate nitrate (at 1549 cm⁻¹) [47]. After the further introduction of NH_3 , the bands of bridging nitrate and bidentate nitrate decreased and disappeared in 3 min. At the same time, the bands at 1415 cm⁻¹ attributed to ionic NH_4^+ and coordinated NH_3 (at 1261 cm⁻¹) appeared after 3 min, indicating that both bridging nitrate and bidentate nitrate could react with NH_3 [48,52]. Based on Figs. 9 b and S6d, the amount of nitrate species on mesoporous $\text{WO}_3(1)\text{-CeO}_2$ surface was higher than that on bulk $\text{WO}_3(1)\text{-CeO}_2$ surface, suggesting that mesoporous $\text{WO}_3(1)\text{-CeO}_2$ should be an excellent material to carry out the $\text{NH}_3\text{-SCR}$ reaction. Compared mesoporous $\text{WO}_3(1)\text{-CeO}_2$ (Fig. 9b) with mesoporous CeO_2 (Fig. S6b), it can be found that doping W brought in more acid sites, which was beneficial for the adsorption of NH_3 species, and thus enhanced the low-temperature activity [15]. Therefore, it can be concluded that enough adsorption amount of nitrate species and NH_3 species was conducive to the higher $\text{NH}_3\text{-SCR}$ activity of mesoporous $\text{WO}_3(1)\text{-CeO}_2$.

3.4.4. Reactions between $\text{NO} + \text{O}_2$ and adsorbed NH_3 species

The reactivity of preadsorbed NH_3 with $\text{NO} + \text{O}_2$ species was also studied on mesoporous $\text{WO}_3(1)\text{-CeO}_2$ by use of *in situ* DRIFTS at 200 °C, which was measured as a function of time (Fig. 9d). After introducing $\text{NO} + \text{O}_2$, the bands at 1402 cm⁻¹ attributed to ionic NH_4^+ , 1592, 1543 and 1245 cm⁻¹ ascribed to coordinated NH_3 decreased obviously in intensity [49,52]. Moreover, all of the bands were substituted by nitrate species after 7 min, suggesting that both coordinated NH_3 and ionic NH_4^+ on mesoporous $\text{WO}_3(1)\text{-CeO}_2$ surface could decrease the amount of NO_x . Although coordinated NH_3

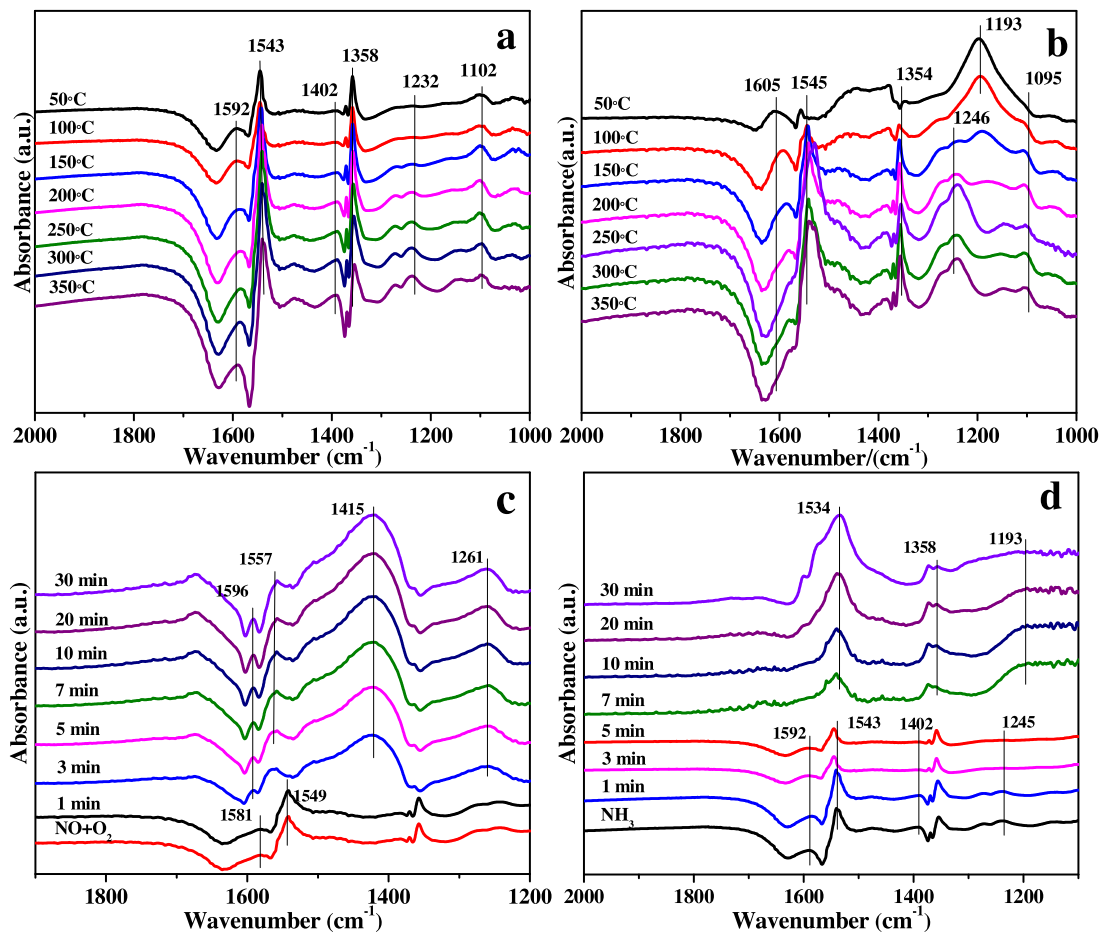
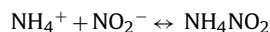


Fig. 9. *In situ* DRIFT spectra of (a) NH₃ adsorption after the catalyst was exposed to a flow of 500 ppm of NH₃ for 30 min and (b) NO + O₂ adsorption after the catalyst was exposed to a flow of 500 ppm of NO + 5% O₂ for 30 min on mesoporous WO₃(1)-CeO₂ as a function of temperature; *in situ* DRIFT spectra of (c) passing NH₃ over NO + O₂ preadsorbed mesoporous WO₃(1)-CeO₂, and (d) passing NO + O₂ over NH₃ preadsorbed mesoporous WO₃(1)-CeO₂ at 200 °C.

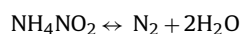
on mesoporous WO₃(1)-CeO₂ surface was important for high SCR activity, ionic NH₄⁺ could also participate in the SCR reaction [51]. Therefore, it indicated that the addition of WO₃ to mesoporous CeO₂ could produce more coordinated NH₃ and ionic NH₄⁺, both of which could play a significant role in the NH₃-SCR reaction.

4. Reaction mechanism

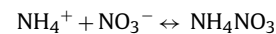
The above analysis results and *in situ* DRIFT spectra study demonstrated that the reaction of adsorbed monodentate NO₃⁻ with adsorbed NH₃ was attributed to the Langmuir-Hinshelwood mechanism at low temperatures on the surface of mesoporous WO₃(1)-CeO₂ (Fig. 10). The NH₃-SCR reaction mechanism was proposed that NH₃(g) was adsorbed on the surface of Lewis acid sites and Brønsted acid sites in the shape of NH₄⁺ ions and gaseous NH₃. Besides, the adsorption of NO could exist in the form of gaseous or oxide ions NO₂⁻ on the surface of mesoporous WO₃(1)-CeO₂ according to the DRIFT spectra. Compared to the adsorption of NO + O₂, the adsorption of NH₃ was stronger. The adsorbed NH₃ species could react with NO₂⁻ species easily to produce NH₄NO₂ via the following reaction:



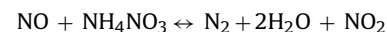
The NH₄NO₂ was extremely unstable and rapidly decomposed into the innocuous N₂ and H₂O according to the reaction:



On the other hand, the adsorbed NO₂⁻ could be oxidized to monodentate NO₃⁻ to proceed in the subsequent reaction. And then NH₄⁺ ions reacted with monodentate NO₃⁻ on active sites to generate NH₄NO₃.



The NH₄NO₃ formation has been observed in many other SCR catalyst systems, which was reported relatively stable at low temperature. Therefore, it may block the active sites of the SCR reaction. If the temperature was higher than 200 °C, NH₄NO₃ could decompose to N₂O and H₂O. N₂O was considered as an intermediate product during the process of SCR reaction, which can be activated into N-NO or NN-O [47,50]. Noteworthily, comparing mesoporous CeO₂ and pure WO₃ with mesoporous WO₃(1)-CeO₂, the amount of N₂O on the surface of mesoporous WO₃(1)-CeO₂ decreased, indicating that most of NH₄NO₃ reacted with NO on mesoporous WO₃(1)-CeO₂ surface by the following reaction:



The reaction was considered to be decisive in the process of NH₃-SCR reaction since it could remove surface NH₄NO₃ and continuously transform NO into N₂. The NO₂ that simultaneously formed could be adsorbed again and reacted with NH₃ [51,52]. Besides, only a negligible amount of N₂O was detected under NH₃-SCR reaction conditions, indicating that the NH₄NO₃ decomposition reaction was not significant. That is to say, once NH₄NO₃ species formed under NH₃-SCR conditions, it would decrease

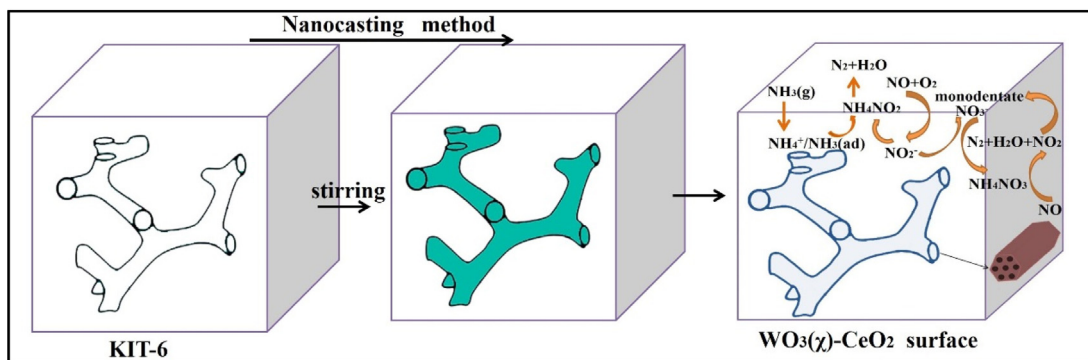


Fig. 10. The NH_3 -SCR reaction mechanism on $\text{WO}_3(\chi)$ - CeO_2 surface at low temperature.

quickly due to the reaction with excess NO . Therefore, it was not observed on the surface of mesoporous $\text{WO}_3(1)$ - CeO_2 through *in situ* DRIFTS.

5. Conclusions

In this work, highly ordered mesoporous $\text{WO}_3(\chi)$ - CeO_2 nanomaterials have been synthesized by using KIT-6 as the hard template and applied in the NH_3 -SCR reaction to remove NO_x . The NO_x conversion efficiency reached 100% at a wider temperature window from 225 to 350 °C. In order to explore the reaction mechanism, mesoporous CeO_2 , bulk $\text{WO}_3(\chi)$ - CeO_2 and commercial V_2O_5 - WO_3 / TiO_2 were compared with mesoporous $\text{WO}_3(\chi)$ - CeO_2 . It can be found that mesoporous $\text{WO}_3(1)$ - CeO_2 exhibited the best NH_3 -SCR activity in wider operating temperature window, superior water-resistance effect, better alkali metal poisoning resistance, higher stability and a relatively high N_2 selectivity at low temperature, which was due to its ordered mesoporous structure, the higher $\text{Ce}^{3+}/\text{Ce}^{4+}$ mole ratio, enough surface chemisorbed oxygen and the much more amount of Lewis acid sites. Therefore, mesoporous $\text{WO}_3(1)$ - CeO_2 catalyst has great potential for industrial applications in controlling NO_x emissions.

Acknowledgements

The authors gratefully acknowledge the financially support by Natural Science Foundation of China (21377061, 81270041), and Key Technologies R&D Program of Tianjin (15JCZBJC48400, 14ZCZDSF00001, 15JCZDJC41200 and 16YFZCSF00300). Financial support from NIH (R21AI107415 and SC2GM105584), UT STARS Award, BBRC Pilot and IDR2 Award from UTEP is also gratefully acknowledged.

Appendix A. Supplementary data

Supplementary data associated with this article can be found, in the online version, at <http://dx.doi.org/10.1016/j.apcatb.2016.10.010>.

The other related figures and data about the $\text{WO}_3(\chi)$ - CeO_2 materials, such as N_2 adsorption-desorption isotherms and pore diameter distribution, XPS spectrum, SO_2 tolerance and *in situ* DRIFT spectra. This material is available free of charge via the Internet at <http://pubs.acs.org>.

References

- [1] B. Zhi, H. Ding, D. Wang, Y. Cao, Y. Zhang, X. Wang, Y. Liu, Q. Huo, J. Mater. Chem. A 2 (2014) 2374–2382.
- [2] H. Chang, M. Jong, C. Wang, R. Qu, Y. Du, J. Li, J. Hao, Environ. Sci. Technol. 47 (2013) 11692–11699.
- [3] X. Xie, Y. Li, Z. Liu, M. Haruta, W. Shen, Nature 458 (2009) 746–749.
- [4] J. Li, H. Chang, L. Ma, J. Hao, R. Yang, Catal. Today 175 (2011) 147–156.
- [5] Y. Peng, J. Li, W. Shi, J. Xu, J. Hao, Environ. Sci. Technol. 46 (2012) 12623–12629.
- [6] B. Shen, Y. Wang, F. Wang, T. Liu, Chem. Eng. J. 236 (2014) 171–180.
- [7] H. Chang, X. Chen, J. Li, L. Ma, C. Wang, C. Liu, W.S. Johannes, J. Hao, Environ. Sci. Technol. 47 (2013) 5294–5301.
- [8] J. Li, S. Li, J. Phys. Chem. C 112 (2008) 16938–16944.
- [9] J. Liu, X. Wu, S. Zou, Y. Dai, L. Xiao, X. Gong, J. Fan, J. Phys. Chem. C 118 (2014) 24950–24958.
- [10] J. Strunk, W.C. Vining, A.T. Bell, J. Phys. Chem. C 115 (2011) 4114–4126.
- [11] D. Kwon, K. Nam, S. Hong, Appl. Catal. B 166–167 (2015) 37–44.
- [12] K. Wijayanti, A. Kumar, S. Joshi, K. Kamamudram, N.W. Currier, A. Yezerets, L. Olsson, Appl. Catal. B 163 (2015) 382–392.
- [13] X. Auvray, W. Partridge, J. Choi, J. Pihl, F. Coehlo, A. Yezerets, K. Kamamudram, N. Currier, L. Olsson, Appl. Catal. B 163 (2015) 393–403.
- [14] S. Yang, Y. Liao, S. Xiong, F. Qi, H. Dang, X. Xiao, J. Li, J. Phys. Chem. C 118 (2014) 21500–21508.
- [15] Y. Peng, J. Li, L. Chen, J.H. Chen, J. Han, H. Zhang, W. Han, Environ. Sci. Technol. 46 (2012) 2864–2869.
- [16] S. Shwana, J. Jansson, L. Olsson, M. Skoglundh, Appl. Catal. B 166–167 (2015) 277–286.
- [17] M. Casanova, L. Nodari, A. Sagar, K. Schermanz, A. Trovarelli, Appl. Catal. B 176–177 (2015) 699–708.
- [18] J. Yu, Z. Si, L. Chen, X. Wu, D. Weng, Appl. Catal. B 163 (2015) 223–232.
- [19] W. Shan, F. Liu, H. He, X. Shi, C. Zhang, Chem. Commun. 47 (2011) 8046–8048.
- [20] W. Shan, F. Liu, H. He, X. Shi, C. Zhang, Appl. Catal. B 115–116 (2012) 100–106.
- [21] L. Chen, J. Li, W. Ablikim, J. Wang, H. Chang, L. Ma, J. Xu, M. Ge, H. Arandiyan, Catal. Lett. 141 (2011) 1859–1864.
- [22] Y. Peng, K. Li, J. Li, Appl. Catal. B 140–141 (2013) 483–492.
- [23] B. Hu, H. Liu, K. Tao, C. Xiong, S. Zhou, J. Phys. Chem. C 117 (2013) 26385–26395.
- [24] C. Liu, L. Chen, J. Li, L. Ma, H. Arandiyan, Y. Du, J. Xu, J. Hao, Environ. Sci. Technol. 46 (2012) 6182–6189.
- [25] J. Luo, J. Zhang, Y. Xia, Chem. Mater. 18 (2006) 5618–5623.
- [26] P. Ji, J. Zhang, F. Chen, M. Anpo, J. Phys. Chem. C 112 (2008) 17809–17813.
- [27] C. Ho, J. Yu, T. Kwong, A.C. Mak, S. Lai, Chem. Mater. 17 (2005) 4514–4522.
- [28] R.M. Serra, S.G. Aspromonte, E.E. Miró, A.V. Boix, Appl. Catal. B 166–167 (2015) 592–602.
- [29] C. Gao, Y. Lin, Y. Li, D.G. Evans, D. Li, Ind. Eng. Chem. Res. 48 (2009) 6544–6549.
- [30] Y. Chang, K. Yu, C. Zhang, R. Li, P. Zhao, L. Lou, S. Liu, Appl. Catal. B 176 (2015) 363–373.
- [31] Z. Ma, X. Wu, Y. Feng, Z. Si, D. Weng, Catal. Commun. 69 (2015) 188–192.
- [32] R. Qu, X. Gao, K. Cen, J. Li, Appl. Catal. B 142–143 (2013) 290–297.
- [33] J. Xu, P. Li, X. Song, C. He, J. Yu, Y. Han, J. Phys. Chem. Lett. 1 (2010) 1648–1654.
- [34] A. Mamede, E. Payen, P. Grange, G. Poncelet, A. Ion, M. Alifanti, V. Parvulescu, J. Catal. 223 (2004) 1–12.
- [35] J. Deng, L. Zhang, H. Dai, Y. Xia, H. Jiang, H. Zhang, H. He, J. Phys. Chem. C. 114 (2010) 2694–2700.
- [36] C. Hahn, M. Endisch, F.J. Schottb, S. Kuretia, Appl. Catal. B 168–169 (2015) 429–440.
- [37] P. Li, Y. Xin, Q. Li, Z. Wang, Z. Zhang, L. Zheng, Environ. Sci. Technol. 46 (2012) 9600–9605.
- [38] P. Wang, H. Wang, X. Chen, Y. Liu, X. Weng, Z. Wu, J. Mater. Chem. A 3 (2015) 680–690.
- [39] Z. Liu, J. Zhu, J. Li, L. Ma, S. Woo, ACS Appl. Mater. Interfaces 6 (2014) 14500–14508.
- [40] P. Maitarad, J. Han, D. Zhang, L. Shi, S. Namuangruk, T. Rungrotmongkol, J. Phys. Chem. C 118 (2014) 9612–9620.
- [41] L. Chen, J. Li, M. Ge, Chem. Eng. J. 170 (2011) 531–537.
- [42] Z. Huang, H. Li, J. Gao, X. Gu, L. Zheng, P. Hu, Y. Xin, J. Chen, Y. Chen, Z. Zhang, J. Chen, X. Tang, Environ. Sci. Technol. 49 (2015) 14460–14465.
- [43] Y. Shi, H. Shu, Y. Zhang, H. Fan, Y. Zhang, L. Yang, Fuel Process. Technol. 150 (2016) 141–147.
- [44] L. Chen, J. Li, M. Ge, Environ. Sci. Technol. 44 (2010) 9590–9596.

- [45] R. Gao, D. Zhang, P. Maitarad, L. Shi, T. Rungrotmongkol, H. Li, J. Zhang, W. Cao, *J. Phys. Chem. C* 117 (2013) 10502–10511.
- [46] Y. Liu, T. Gu, X. Weng, Y. Wang, Z. Wu, H. Wang, *J. Phys. Chem. C* 116 (2012) 16582–16592.
- [47] H. Hu, S. Cai, H. Li, L. Huang, L. Shi, D. Zhang, *ACS Catal.* 5 (2015) 6069–6077.
- [48] Y. Liu, J. Xu, H. Li, S. Cai, H. Hu, C. Fang, L. Shi, D. Zhang, *J. Mater. Chem. A* 3 (2015) 11543–11553.
- [49] L. Zhang, L. Shi, L. Huang, J. Zhang, R. Gao, D. Zhang, *ACS Catal.* 4 (2014) 1753–1763.
- [50] X. Zhang, Q. Shen, C. He, C. Ma, J. Cheng, L. Li, Z. Hao, *ACS Catal.* 2 (2012) 512–520.
- [51] D. Wang, L. Zhang, K. Kamasamudram, W.S. Epling, *ACS Catal.* 3 (2013) 871–881.
- [52] S. Ding, F. Liu, X. Shi, K. Liu, Z. Lian, L. Xie, H. He, *ACS Appl. Mater. Interfaces* 7 (2015) 9497–9506.